

Enhanced densification under shock compression in porous silicon

J. Matthew D. Lane,¹ Aidan P. Thompson,¹ and Tracy J. Vogler²

¹*Sandia National Laboratories, Albuquerque, NM 87185*

²*Sandia National Laboratories, Livermore, CA 94551*

(Dated: June 27, 2014)

Under shock compression, most porous materials exhibit lower densities for a given pressure than that of a full-dense sample of the same material. However, some porous materials exhibit an anomalous, or enhanced, densification under shock compression. The mechanism driving this behavior was not completely determined. We present evidence from atomistic simulation that pure silicon belongs to this anomalous class of materials and demonstrate the associated mechanisms responsible for the effect in porous silicon. Atomistic response indicates that local shear strain in the neighborhood of collapsing pores catalyzes a local solid-solid phase transformation even when bulk pressures are below the thermodynamic phase transformation pressure. This metastable, local, and partial, solid-solid phase transformation, which accounts for the enhanced densification in silicon, is driven by the local stress state near the void, not equilibrium thermodynamics. This mechanism may also explain the phenomenon in other covalently bonded materials.

In most materials the introduction of voids or porosity alters the shock response in a predictable way as compared to the material's full-dense response. Generally, the final high-pressure states of porous materials are hotter and less dense than the corresponding full-dense material compressed to the same final pressure. Hotspot heating during void collapse and crush up significantly drives up temperatures. Thermal expansion then results in lower densities for a given pressure; or conversely, higher pressures for a given density. However, some porous materials exhibit an anomalous response, in which the final shock state of the porous material is denser than the final shock state of the non-porous sample of the same material. A porous material exhibits enhanced densification when its Hugoniot is shifted down and to the right of the principal Hugoniot in a pressure-density representation, as seen in Fig 1.

Enhanced densification has been observed experimentally in silicon dioxide, boron carbide, uranium dioxide and silicon nitride. Grady, Fenton and Vogler [1] have reviewed experimental data, and empirically fit an Equation of State to describe this unusual shock response in brittle high-strength porous materials. However, the underlying mechanism responsible for the effect is not known. Several mechanisms have been proposed which are based on thermodynamic arguments [2], due to increased temperature in the samples. These include a thermally-activated volume-reducing chemical dissociation process, homogeneous lattice contraction due to negative thermal expansion (negative Gruneisen parameter) and an accelerated solid-solid phase transition stimulated by either thermodynamic arguments (increased temperature combined with a negatively sloping T-P transition line) [3], or by mechanical arguments (anisotropic stress state in the vicinity of the voids) [4].

Porous silicon has not previously been identified with enhanced densification, but shares some traits with such materials, (e.g. brittle, high-strength, covalent bonding

and a pressure-induced solid-solid phase transformation). We show in this letter that porous silicon exhibits enhanced densification and, using atomistic molecular dynamics simulations, illustrate the underlying mechanisms which drive the response. We show that, in silicon, local shear deformation resulting from collapsing voids drives a partial phase transition to a higher density phase, and produces anomalously higher final shock densities in initially distended materials.

Silicon's critically important technological role comes mainly from its semiconducting ambient diamond crystal

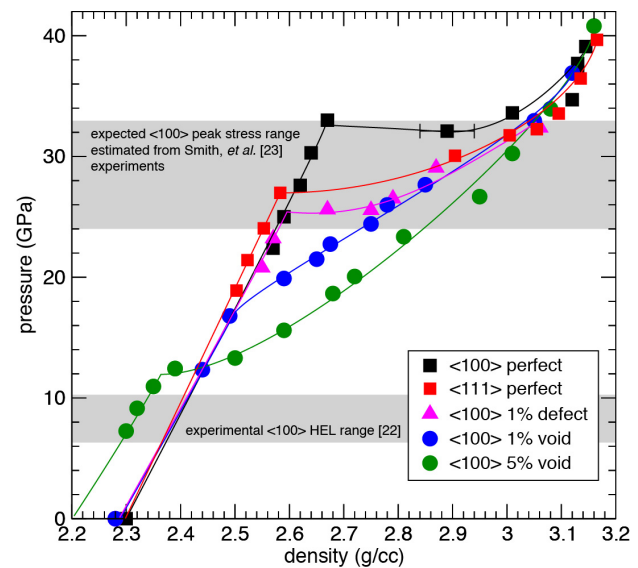


FIG. 1: (Color online) Low porosity silicon Hugoniot curves for 1% (blue circles) and 5% (green circles) shocked along the $\langle 100 \rangle$ orientation from molecular dynamics simulation. The principal Hugoniot curves for defect-free single-crystal silicon shocked along $\langle 100 \rangle$ (black squares) and $\langle 111 \rangle$ (red squares), as well as defective crystal with 1% vacancy (pink triangles) are shown for comparison.

structure. Hydrostatic high-pressure loading produces a low-temperature pressure-induced phase transition near 12 GPa to the metallic body-center-tetragonal (bct), β -tin structure. The transition brings a 21% density increase and change in c/a lattice ratio from 1.44 (dia-

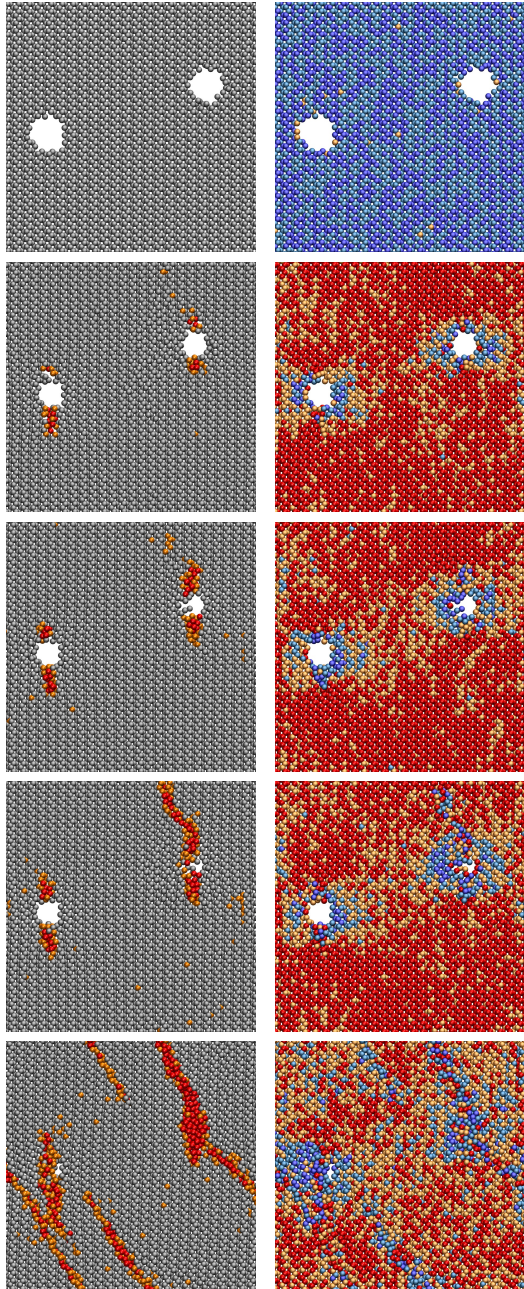


FIG. 2: (Color online) Slices showing evolution (top to bottom) of the atoms around collapsing voids in the 1% void system after a 20 GPa shock wave passes. On the left, atoms are colored for coordination number, an indicator of diamond (gray) to high-density phases (red). On the right, atoms are colored for shear stress, $\tau = P_{zz} - (P_{xx} + P_{yy})/2$, with blue being low τ and red being high. Times were approx. -6 ps, 2 ps, 4 ps, 8 ps, and 44 ps relative to the shock overtake.

mond) to 0.55 (bct). The phase diagram, reported by Bundy [5], and more recently by Voronin *et al.*[6], shows a negatively sloped phase line in T-P space. Moreover, silicon's diamond phase exhibits a negative Gruneisen parameter, or negative thermal expansion. Under uniaxial shock compression, multiple solid-solid transitions have been reported [7, 8], to the high-density β -tin, Imma, or sh structures. Moreover, the transition barriers to these high-pressure phases are lowered under shear, according to DFT calculations [9–11]. Porous crystalline silicon has been produced through high-energy helium implantation and annealing [12, 13]. To our knowledge, no shock loading experiments have been conducted on porous silicon.

Classical molecular dynamics (MD) simulation was used to explore the atomic-scale processes associated with the collapse of voids in porous silicon. MD has been used extensively to study shock compression mechanisms which require the resolution of atomistic detail [14, 15], and is especially useful when heterogeneity [16, 17] requires domain sizes too large for density functional theory (QMD-DFT). Sandia's LAMMPS code [18] was used with the Modified Embedded Atom Method (MEAM) [19] and silicon parameters distributed in LAMMPS as Si97 within library.meam [20, 21]. A complete description of the potential is provided in the supplementary materials [22].

The silicon samples were 13.1 nm x 13.1 nm wide with periodic transverse boundaries, and ranged in length from 320 nm to 1.84 μ m in the shock direction. Shocks were driven with a constant-velocity momentum mirror. Piston velocities ranged from 0.2 to 2.0 km/s. A 0.2 fs time step was used. Samples were pre-equilibrated to 300 kelvins. One-dimensional profiles of density, pressure, temperature, and particle velocity were calculated by averaging per-atom quantities in 0.1 nm wide slabs normal to the wave propagation direction. Here, and throughout this manuscript, pressure refers to the 1D pressure in the propagation direction, the P_{zz} component of the pressure tensor. Final values for the shock wave observables were determined by spatial averages behind the shock front. These final values were consistent with the Rankine-Hugoniot equations, indicating that the shocks had reached a steady state condition.

Varying degrees of porosity were introduced in the silicon samples from perfect crystal to 50% porosity. Perfect lattices contained no vacancy defects or interstitials. A defective crystal was created by removing individual atoms to reduce the density by 1%. Low porosity samples, with densities reduced by 1% and 5%, were created by cutting randomly positioned 2 nm diameter spherical voids and re-equilibrating at 300 K for 10 ps. 2 nm voids were chosen because they were the smallest voids which produced response qualitatively different from the defective crystal – localizing shear strains and nucleating densification under shock. Larger voids behaved similarly, but produced less homogeneity in our small sam-

ples, which was undesirable. High porosity samples, with densities reduced by 25% and 50%, were constructed using two methods. See Figure 3. The first was the void cutting method already described. The second was to aggregate randomly-oriented and randomly-placed 4 nm diameter spheres of silicon single crystal, removing overlap atoms, until the appropriate density was reached.

Figure 1 shows the principal shock Hugoniot results in pressure-density for silicon single crystal along the $\langle 100 \rangle$ and $\langle 111 \rangle$ directions. We see that both exhibit elastic compression followed by a plastic softening, with a peak elastic stress of 33 GPa in $\langle 100 \rangle$ and lower for $\langle 111 \rangle$. These values are in relatively good agreement with high strain-rate ($10^6 - 10^9$ 1/s) compression experiments in silicon by Smith *et al.* [23] which measured peak elastic stresses exceeding twice the Hugoniot Elastic Limits (HELs) measured by Gust and Royce [7]. Extrapolation of the Smith results to MD length and time scale predicts peak elastic stresses in the range from 24 – 33 GPa. This estimate and the experimental $\langle 100 \rangle$ HEL are indicated by gray bands in Figure 1.

Figure 1 also includes the Hugoniot curve for $\langle 100 \rangle$ crystal with 1% vacancy defects. As expected, the introduction of defects lowers the peak elastic stress, but does not qualitatively alter the shock response. In both the perfect and defective crystals we observe that the applied uniaxial strain produces shear stress which, above the onset of plasticity, nucleates a solid-solid phase transition which propagates along planar stacking faults. This shear stress driven partial phase transformation has been observed previously in MD simulations of germanium [24] and very recently in silicon [25]. The higher-density crystal is either a tetragonal (β -tin) or the closely-related orthorhombic (Imma) structure. Definitive determination is difficult due to the small transformed volume and deformation state.

Also in Figure 1 we plot the Hugoniot results for 1% and 5% porosity silicon. We note that the 1% void sample responds significantly differently than the 1% vacancy de-

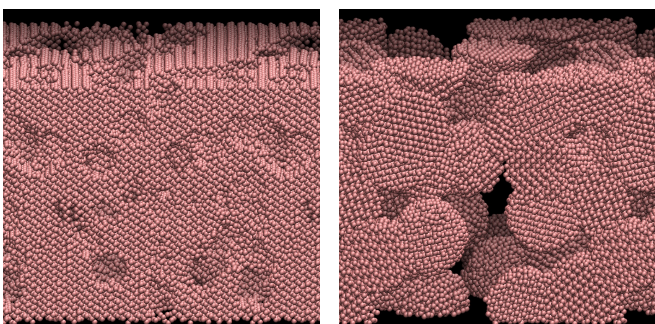


FIG. 3: (Color online) Sample geometries for silicon with 50% porosity. (left) Cut spherical voids from a single crystal; and (right) assembly of polycrystal from randomly oriented spherical grains.

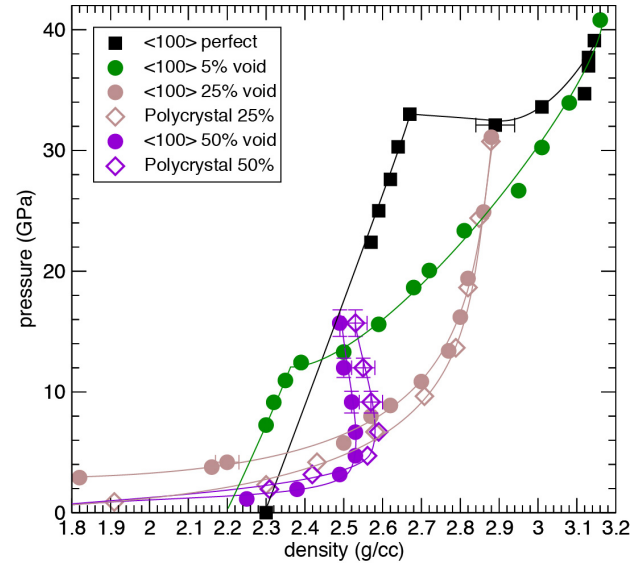


FIG. 4: (Color online) High porosity silicon Hugoniot curves for 25% (brown) and 50% (purple) shocked along the $\langle 100 \rangle$ orientation. Two Hugoniot curves are shown for each porosity representing the cut void (circles) and aggregated polycrystal (diamonds) construction methods. The principal Hugoniot curve for defect-free $\langle 100 \rangle$ single-crystal silicon (black squares) and 5% low porosity (green circles) are shown for comparison.

fective crystal. The voids drive a localized phase transformation in the vicinity of the void. The 1% and 5% porous silicon Hugoniots both show enhanced densification, with Hugoniots crossing below the principal Hugoniot under moderate pressure – a signature of enhanced densification. At pressures above 30 GPa the Hugoniots rejoin the principal Hugoniot, as the samples are driven to partial melt and the effects of the induced solid-solid phase transition is suppressed. Importantly, we see that the void collapse in low porosity silicon does not significantly raise the system temperature or these high pressure Hugoniots would not reconverge. We discuss temperature effects in more detail below.

Figure 2 shows atomistic snapshots of void collapse in the 1% porous silicon colored for crystal structure and shear stress. The images demonstrate the mechanism responsible for the enhanced densification of these porous samples. The top two images show a pair of voids in the uncompressed material. The lower images show how these voids gradually collapse behind the shock front, nucleating partial phase transformation and relieving shear stress. As the pores collapse, local shear stress is relieved by shear strain in the neighborhood of the void. This local shear strain nucleates the transition to the higher density β -tin solid phase. As the pore further collapses, these former low-density regions, become locally more dense than average and the associated shear partially transforms regions to higher density phase, which in turn nucleates ribbons of transformed material extend-

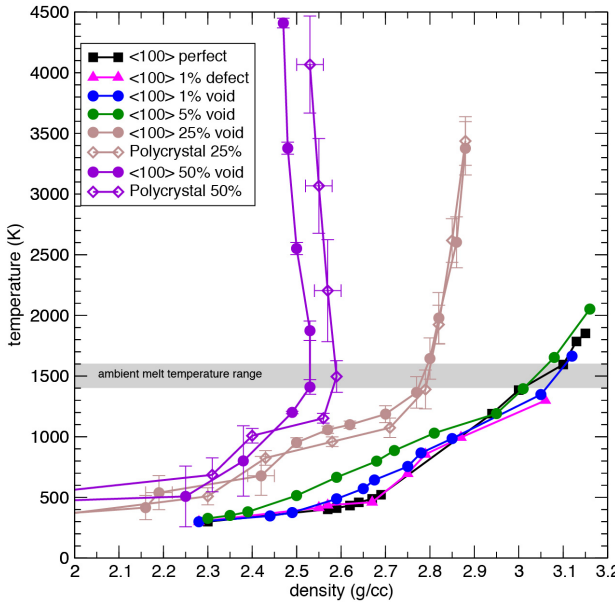


FIG. 5: (Color online) Temperature versus density for silicon with various degrees of initial porosity. Symbols are the same as in Figures 1 and 4.

ing from the collapsed void. In the bottom right image of Figure 2 we see the final state after shock, a partially transformed material with highest density regions replacing voids and bulk crystal untransformed. Thus the energy and shear stress which in most porous materials is lost to heat and leads to expansion, instead drives a local transformation to a higher density phase. We believe this partial transition to be metastable, since local temperatures are below those that would allow either melt or annealing to homogenize these structures.

At higher porosities of 25% and 50%, we see an even stronger effect. As shown in Figure 4, higher porosity means more locally transformed regions and therefore an overall higher density for a given pressure. As discussed earlier, two methods were used to construct these highly porous structures. At 50% porosity we see almost no dependence on the different structures, while at 25% porosity, we see some indication of slightly higher strength in the cut voids sample. However, here too, the two curves come together at higher pressure. All high porosity samples exhibit sharp steepening at higher shock intensities, with the 50% porous samples even turning back to lower densities. This effect is also seen in experiments [1] for very distended materials and is due to the effect of shock temperature increases, which ultimately drive expansion of the sample. For high initial distentions, the maximum density can be lower than the ambient crystal density.

Figure 5 shows the final temperature as a function of density for shock compression of all systems. The temperatures rise steeply for the 25% and 50% porous silicon. In these two cases, the void collapse ultimately leads to

large and rapid increases in temperature. However, for lower porosity, the increases compared to the full-dense material (black squares in Fig. 5) are quite modest. This indicates that temperature does not play a significant role in the enhanced densification we observe at low porosities. The solid-solid phase transition is driven by the local stress environment rather than thermodynamics, and the transformation appears to act as an energy sink for energy that would normally go toward system heating. At higher porosities this mechanism is overwhelmed, and this leads to the rapid temperature increases seen in the 25% and 50% porosity silicon.

In conclusion, we have identified porous silicon to be in a class of materials which exhibit enhanced densification under shock compression. Further, we have identified the mechanism by which this enhanced densification can be explained, using atomistic molecular dynamics. The primary mechanism is through local solid-solid phase transition in the vicinity of collapsing voids to a denser solid phase. Moreover, we show that this partial phase transition is driven by the local stress state around these voids, and is not due to a thermodynamic explanation based on significantly increased temperature. These findings imply that enhanced densification of porous materials may be more common than realized in brittle materials with large-volume solid/solid phase transitions and high strength.

This work was supported in part by the Laboratory Directed Research and Development (LDRD) Program at Sandia. Sandia National Laboratories is a multiprogram laboratory managed and operated by Sandia Corporation, a wholly owned subsidiary of Lockheed Martin Corporation, for the U.S. Department of Energy's National Nuclear Security Administration under contract DE-AC04-94AL85000.

- [1] D. Grady, G. Fenton, and T. Vogler, *Int. J. Impact Eng.* (2012).
- [2] A. B. Medvedev and R. F. Trunin, *Phys.-Uspekhi* **55**, 773 (2012).
- [3] V. Yakushev, A. Utkin, and A. Zhukov, *AIP SCCM Conf. Proc.* **1426**, 1529 (2012).
- [4] D. Grady, *J. Geophys. Res.* **85**, 913 (1980).
- [5] F. Bundy, *J. Chem. Phys.* **41**, 3809 (1964).
- [6] G. Voronin, C. Pantea, T. Zerda, L. Wang, and Y. Zhao, *Phys. Rev. B* **68**, 020102 (2003).
- [7] W. Gust and E. Royce, *J. Appl. Phys.* **42**, 1897 (1971).
- [8] S. J. Turneaure and Y. Gupta, *Appl. Phys. Lett.* **91**, 201913 (2007), and *Appl. Phys. Lett.* **90**, 051905 (2007).
- [9] C. Cheng, W.-H. Huang, and H. Li, *Phys. Rev. B* **63**, 153202 (2001).
- [10] K. Gaál-Nagy and D. Strauch, *Phys. Rev. B* **73**, 134101 (2006).
- [11] R. Hennig, A. Wadehra, K. Driver, W. Parker, C. Umrigar, and J. Wilkins, *Phys. Rev. B* **82**, 014101 (2010).

- [12] S. Frabboni, F. Corni, C. Nobili, R. Tonini, and G. Ottaviani, Phys. Rev. B **69**, 165209 (2004).
- [13] V. Raineri, M. Saggio, and E. Rimini, J. of Mater. Res. **15**, 1449 (2000).
- [14] B. L. Holian and P. S. Lomdahl, Science **280**, 2085 (1998).
- [15] K. Kadau, T. C. Germann, P. S. Lomdahl, and B. L. Holian, Science **296**, 1681 (2002).
- [16] S. Traiviratana, E. M. Bringa, D. J. Benson, and M. A. Meyers, Acta Mater. **56**, 3874 (2008).
- [17] J. M. D. Lane, G. S. Grest, and T. R. Mattsson, Comp. Mater. Sci. **79**, 873 (2013), and S. Root et al., J. Appl. Phys. **114**, 103502 (2013).
- [18] S. J. Plimpton, J. Comp. Phys. **117**, 1 (1995), LAMMPS code <http://lammps.sandia.gov>.
- [19] M. Baskes, Phys. Rev. B **46**, 2727 (1992), and M. Baskes and R. Johnson, Model. Sim. Mater. Sci. Eng. **2**, 147 (1994).
- [20] M. I. Baskes, Model. Sim. Mater. Sci. Eng. **5**, 149 (1997).
- [21] N. Badis, H. Feraoun, H. Aourag, and M. Certier, Mater. Chem. Phys. **80**, 405 (2003).
- [22] Supplemental materials available at: <http://XXX>.
- [23] R. Smith, R. Minich, R. Rudd, J. Eggert, C. Bolme, S. Bryggo, A. Jones, and G. Collins, Phys. Rev. B **86**, 245204 (2012).
- [24] J. M. D. Lane and A. P. Thompson, AIP SCCM Conf. Proc. **1195**, 1157 (2009).
- [25] G. Mogni, A. Higginbotham, K. Gaál-Nagy, N. Park, and J. S. Wark, Phys. Rev. B **89**, 064104 (2014).

Supplemental Material for Enhanced densification under shock compression in porous silicon

J. Matthew D. Lane,¹ Aidan P. Thompson,¹ and Tracy J. Vogler²

¹*Sandia National Laboratories, Albuquerque, NM 87185*

²*Sandia National Laboratories, Livermore, CA 94551*

The Modified Embedded Atom Method (MEAM) was developed by Baskes *et al.* in a series of papers [1–3] and has been implemented in LAMMPS as an optional package. MEAM computes energies using a semi-empirical combination of two-body interaction and environment-specific electron density embedding energies. MEAM can model covalent bonding by introducing angle-dependent electron densities.

The MEAM potential has been widely used for shock simulations [4–8]. The parameters we used, Table I, are distributed in the LAMMPS package as Si97 in library.meam. These parameters are from Baskes [3] and have been widely applied. Yamaghishi *et al.* [9] used it to study surface reconstructions in silicon. Heino [10] used it to study strength at interfaces. Badis *et al* [11] used it in a study of silicon’s more exotic high-pressure crystal structures.

The atom embedding attempts to account for the electron density surrounding an atom. As atom density increases, the electron density becomes a function of many atoms and the embedding energy therefore becomes an effective environment-dependent interaction. The environment-dependent nature of MEAM makes it especially good for applications near surfaces, voids and interfaces. In these regions, where the local environment is very different from the bulk environment, potentials are usually at their weakest, having been parameterized with bulk measurements.

The total energy given by MEAM is

$$E = \sum_i \left(F(\bar{\rho}_i) + \frac{1}{2} \sum_{j \neq i} \phi(R_{ij}) \right) \quad (1)$$

where the sums are over particle indices; F is the embedding energy as a function of $\bar{\rho}_i$, the background electron density at the site of the i^{th} particle; and ϕ is the two-body interaction between particles i and j as a function of R_{ij} .

The embedding function, F , has the form

$$F(\bar{\rho}_i) = A E_c \bar{\rho}_i \ln \bar{\rho}_i \quad (2)$$

where A is a parameter and E_c is the cohesive energy. The background electron density is calculated at each site by

$$\bar{\rho} = \rho^{(0)} G(\Gamma) \quad (3)$$

where $\rho^{(0)}$ is the partial electron density of spherically symmetric s orbital contributions from surrounding atoms

$$\rho^{(0)} = \sum_i \rho^{a(0)}(r_i) \quad (4)$$

and G is a material specific function of Γ , which is itself a function of $\rho^{(1)}$, $\rho^{(2)}$, and $\rho^{(3)}$, the angular dependent partial electron densities associated with the p, f and g orbitals, respectively.

$$G(\Gamma) = \sqrt{1 + \Gamma} \quad (5)$$

$$\Gamma = \sum_{h=1}^3 t^{(h)} \left(\frac{\rho^{(h)}}{\rho^{(0)}} \right)^2 \quad (6)$$

E^0	R^0	r_c	α	A	$\beta^{(0)}$	$\beta^{(1)}$	$\beta^{(2)}$	$\beta^{(3)}$	$t^{(0)}$	$t^{(1)}$	$t^{(2)}$	$t^{(3)}$
4.63	2.35	4.0	4.87	1.0	4.4	5.5	5.5	5.5	1.0	3.13	4.47	-1.8

TABLE I: MEAM Parameters for silicon (in eV, Å units) as in LAMMPS library.meam element Si97 and Ref. [3].

where Γ is a weighted sum of the non-spherically symmetric partial electron densities. $t^{(1)}$, $t^{(2)}$, and $t^{(3)}$ are parameters indicating the relative importance of each orbital, and the higher partial electron densities are

$$\left(\rho^{(1)}\right)^2 = \sum_{\alpha} \left[\sum_i \rho^{a(1)}(r_i) \frac{r_{i\alpha}}{r_i} \right]^2 \quad (7)$$

$$\left(\rho^{(2)}\right)^2 = \sum_{\alpha, \beta} \left[\sum_i \rho^{a(2)}(r_i) \frac{r_{i\alpha} r_{i\beta}}{(r_i)^2} \right]^2 - \frac{1}{3} \left[\sum_i \rho^{a(2)}(r_i) \right]^2 \quad (8)$$

$$\left(\rho^{(3)}\right)^2 = \sum_{\alpha, \beta, \gamma} \left[\sum_i \rho^{a(3)}(r_i) \frac{r_{i\alpha} r_{i\beta} r_{i\gamma}}{(r_i)^3} \right]^2 \quad (9)$$

where α , β and γ run through the coordinates, and $r_{i\alpha}$ is the α -component of r_i . Each of the $\rho^{a(h)}(r)$ are the atomic electron densities, which decay exponentially with distance

$$\rho^{a(h)}(r) = e^{-\beta^{(h)}(r/r_e - 1)} \quad (10)$$

where h is an integer from 1 to 3, $\beta^{(1)}$, $\beta^{(2)}$, $\beta^{(3)}$ are parameters, and r_e is the nearest neighbor distance in a material specific pre-defined reference structure.

The second term from the MEAM total energy, Equation 1, is the two-body interaction term

$$\phi(R) = \frac{2}{Z} \{ E^u(R) - F(\bar{\rho}^0(R)) \} \quad (11)$$

where Z is the number of nearest neighbors in the reference structure and $F(\bar{\rho}^0(R))$ is the embedding energy of the reference structure background electron density $\bar{\rho}^0$. $E^u(R)$ is the energy per atom in the reference structure as a function of the nearest-neighbor distance R .

$$E^u(R) = -E_c(1 + \alpha(R/r_e - 1))e^{-\alpha(R/r_e - 1)} \quad (12)$$

where $\alpha = \sqrt{\frac{9\Omega B}{E_c}}$, and Ω and B are the atomic volume and bulk modulus of the reference structure, respectively.

In lieu of a potential cutoff distance, MEAM implements a many-body screening. The screening function $0 \leq \zeta_{ik} \leq 1$ multiplies the electron densities and the pair potential. The degree of screening is determined by

$$\zeta_{ik} = \prod_{j \neq i, k} S_{ijk} \quad (13)$$

where S_{ijk} is the screening effect of j between the i^{th} and j^{th} particles. S_{ijk} is given by

$$S_{ijk} = f_c \left[\frac{C - C_{\min}}{C_{\max} - C_{\min}} \right] \quad (14)$$

$$f_c(x) = \begin{cases} 1 & x \geq 1 \\ [1 - (1 - x)^4]^2 & 0 < x < 1 \\ 0 & x \leq 0 \end{cases} \quad (15)$$

$$C = \frac{2 \left(\left(\frac{r_{ik}}{r_{ij}} \right)^2 + \left(\frac{r_{kj}}{r_{ij}} \right)^2 \right) - \left(\left(\frac{r_{ik}}{r_{ij}} \right)^2 - \left(\frac{r_{kj}}{r_{ij}} \right)^2 \right)^2 - 1}{1 - \left(\left(\frac{r_{ik}}{r_{ij}} \right)^2 - \left(\frac{r_{kj}}{r_{ij}} \right)^2 \right)^2} \quad (16)$$

where r_{ij} , r_{ik} and r_{kj} are the separation distances between the indexed particles.

[1] M. Baskes, Phys. Rev. B **46**, 2727 (1992).

- [2] M. Baskes and R. Johnson, *Model. Sim. Mater. Sci. Eng.* **2**, 147 (1994).
- [3] M. I. Baskes, *Model. Sim. Mater. Sci. Eng.* **5**, 149 (1997).
- [4] K. Kadau, F. J. Cherne, R. Ravelo, and T. C. Germann, *Phys. Rev. B* **88**, 144108 (2013).
- [5] S. Bernard and J. Maillet, *Phys. Rev. B* **66**, 012103 (2002).
- [6] V. Dremov, A. Karavaev, F. Sapozhnikov, M. Vorobyova, and L. Soulard, **11**, 837 (2009).
- [7] A. P. Thompson, J. M. D. Lane, M. P. Desjarlais, and M. I. Baskes, **1195**, 833 (2009).
- [8] N. Gunkelmann, E. M. Bringa, K. Kang, G. J. Ackland, C. J. Ruestes, and H. M. Urbassek, *Phys. Rev. B* **86**, 144111 (2012).
- [9] T. Yamaghishi, K. Takahashi, and T. Onzawa, *Surf. Sci.* **445**, 18 (2000).
- [10] P. Heino and E. Ristolainen, *Microelectronics Reliability* **43**, 645 (2003).
- [11] N. Badis, H. Feraoun, H. Aourag, and M. Certier, *Mater. Chem. Phys.* **80**, 405 (2003).